Lab-based multi-wavelength EUV diffractometry for critical dimension metrology

Bryan M. Barnes[a], Aaron Chew[b], Nicholas W. Jenkins[c], Yunzhe Shao[c], Martin Y. Sohn[a], R. Joseph Kline[d], Daniel F. Sunday[d], Purnima P. Balakrishnan[b], Thomas A. Germer[b], Steven E. Grantham[b], Clay Klein[c], Stephanie L. Moffitt[b], Eric L. Shirley[b], Henry C. Kapteyn[e], and Margaret M. Murnane[c]

[a]Nanoscale Device Characterization Division, National Institute of Standards and Technology, 100 Bureau Drive MS 6832, Gaithersburg, MD 20899, USA
[b]Sensor Science Division, National Institute of Standards and Technology, 100 Bureau Drive, Gaithersburg, MD 20899, USA
[c]STROBE NSF Science and Technology Center, JILA, University of Colorado, Boulder, CO, 80309 USA
[d]Materials Science and Engineering Division, National Institute of Standards and Technology, 100 Bureau Drive, Gaithersburg, MD 20899, USA
[e]KMLabs, Boulder, CO, 80309 USA

ABSTRACT

Background: The industry is developing extreme-ultraviolet wavelength (EUV) techniques to measure critical dimensions (CDs) in logic fabrication. As nascent approaches are unveiled, evaluations against reference metrologies are essential to motivate development at higher speeds using industrially relevant length scales.
Aim: The parametric geometries determined from EUV diffractometry data using a tabletop coherent high-harmonic generation (HHG) source are compared against dimensions from synchrotron-based CD small angle x-ray scattering (CD-SAXS) for four line-space arrays with CDs below 50 nm.
Approach: An EUV imaging reflectometer captures the 0th order reflection and the 1st order diffraction intensities as functions of grazing angle. The 1st order intensities are functions of five wavelengths from the spectral comb of this HHG source. Fits to these data using rigorous couple-wave analysis (RCWA) electromagnetic simulations yield parametric values and uncertainties.
Results: EUV diffractometry simulations match well in general with the measured data after accounting for cross-sectional geometry and experimental conditions. EUV diffractometry line widths correlate well against those of CD-SAXS at the mid-height of the latter.
Conclusions: These promising results were obtained using a general-purpose prototype coherent EUV reflectometer. Routes for further enhancing the sensitivity and accuracy are presented and are in progress.

Keywords: extreme ultraviolet (EUV), EUV diffractometry, EUV scatterometry, critical dimension small angle x-ray scattering (CD-SAXS)

1. INTRODUCTION

Scatterometry is widespread throughout semiconductor manufacturing for critical dimension (CD) metrology due to its inherently nondestructive nature and its speed relative to scanning probe metrologies. Scatterometry harnesses the polarization control and analysis of incident and reflected visible and ultraviolet (UV) light to

Send correspondence to B.M.B. E-mail: bmbarnes@nist.gov, Telephone: 1 (301) 975 3947
*Certain equipment, instruments, software, or materials are identified in this paper in order to specify the experimental procedure adequately. Such identification is not intended to imply recommendation or endorsement of any product or service by NIST, nor is it intended to imply that the materials or equipment identified are necessarily the best available for the purpose.

Metrology, Inspection, and Process Control XXXIX, edited by Matthew J. Sendelbach, Nivea G. Schuch, Proc. of SPIE Vol. 13426, 134261V · © 2025 SPIE
0277-786X · doi: 10.1117/12.3050342

enable deep sub-wavelength dimensional metrology, pairing experimental results and electromagnetic simulations indexed to a parametrization of its geometry. However, visible and UV scatterometry for nanosheet transistors is proving to be challenging. Current optical CD (OCD) methods cannot adequately interrogate upcoming logic architectures.[1]

The extreme ultraviolet (EUV) spectral region shows promise for non-destructive metrology, including CD metrology. The much shorter wavelengths yield not only reflection but also diffraction for periodic structures at industrially relevant pitches, while coherent EUV high-harmonic generation (HHG) sources also enable polarization control that can benefit scatterometry.[2,3] While several CD metrology experiments have been reported using EUV from synchrotron radiation[4–6] and from discharge-produced plasmas,[6,7] there is an increasing number of reports using in-laboratory, coherent EUV HHG sources,[8–16] often denoting diffractometry as "EUV Scatterometry." This is attracting interest from industry[10–12,14–17] to harness EUV wavelengths. A team at the National Institute of Standards and Technology (NIST) is currently pursuing *both* approaches for EUV CD metrology: The first is a proposed extension of Mueller matrix spectroscopic ellipsometry for wavelengths down to 50 nm that is in development;[18–20] the second is EUV diffractometry in collaboration with the University of Colorado-Boulder using EUV HHG. For both approaches, the goal is to demonstrate a path towards industrial viability for a non-destructive near-line or in-line metrology that could be characterized as the next step beyond OCD metrology at ultraviolet or visible wavelengths.

This work utilizes this latter approach, EUV diffractometry, to measure the nanoscale dimensions of four metrology targets from the AMAG7 reticle.[21] A major goal is the comparison of dimensional measurements from EUV diffraction to critical dimension-small angle x-ray scattering (CD-SAXS) measurements. Fits to the EUV diffractometry measurement data are excellent for three of the four targets used. While some quantitative discrepancies exist at the bottom linewidth and height, in general the cross-sections compare favorably; quantitatively, the CD-SAXS and EUV diffractometry line widths at their half-heights are highly correlated. These promising initial results reveal several improvements that are now required to truly test the potential of laboratory-based EUV diffractometry for semiconductor metrology.

Before presenting these comparisons, we review the experimental apparatus, motivate the interplay between the EUV and these targets, annotate the extraction of data from diffraction patterns, outline our parameterization for simulations of these EUV experiments, and also summarize the CD-SAXS experiments. EUV diffraction data from four targets have been fit in parallel to address sample tilt and other experimental variations while capturing dimensional variations. A key EUV width parameter is plotted as a function of CD-SAXS mid-width to demonstrate correlations.

The novel general-purpose EUV reflectometer has already been demonstrated to have high sub-nm accuracy on multiple industry samples, and validated using correlative AFM, SEM and TEM techniques.[12,13,15,16] The main difference between those past measurements and the current sample set are the larger heights of the structures, which leads to a large change in diffracted intensity of the different HHG orders as a function of angle. Multiple wavelengths can be captured simultaneously to assist in reducing parametric correlations. This prototype EUV reflectometer was not initially designed to include an in-situ calibration of the HHG spectrum. Thus, in this study, the relative intensity ratios of the five most intense incident harmonics are inferred by fitting additional parameters.

2. EXPERIMENTAL AND ANALYTICAL METHODS

2.1 EUV diffraction: Methods and measurements

This work has been performed at the University of Colorado-Boulder using an EUV HHG source coupled to an imaging reflectometer as shown in Fig. 1. General details about this source have been provided recently,[12,15] with details specific to this experiment offered as Appendix A; for HHG system performance closer to state-of-the art, please see Kapteyn *et al.*[22] In brief, an ultrafast femtosecond Ti:Sapphire amplifier (KMLabs) with central wavelength $\lambda_{IR} = 795$ nm (photon energy $E_{IR} = 1.55$ eV) is focused into Ar gas (≈ 5.6 kPa (42 Torr)) to produce EUV wavelengths with photon energies around 41.5 eV. The horizontal (s-polarization on sample) polarization of the infrared light is conserved for this EUV radiation. The EUV comb is spectrally filtered using two 45° multilayer mirrors upstream of the target in Fig. 1. The incident EUV beam is, therefore, a comb of

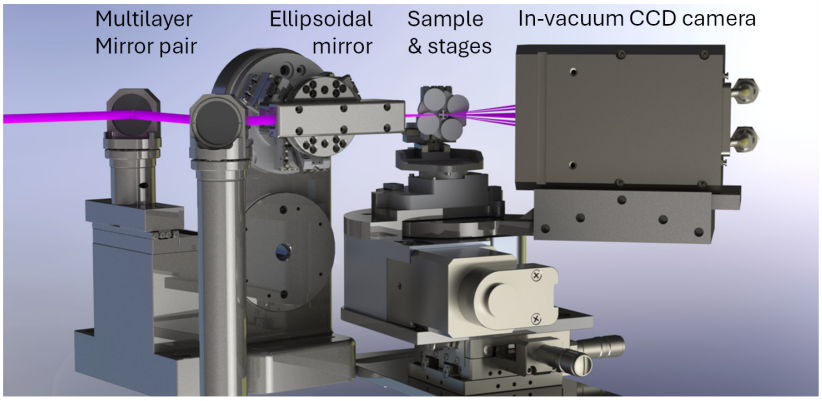

Figure 1. Computer-aided design rendering of the EUV imaging reflectometer. This general-purpose EUV reflectometer was designed for EUV ptychographic coherent diffractive imaging of non-periodic samples.

EUV wavelengths with harmonic $h = 27$ at wavelength (energy) $\lambda_{27} \approx 29\,\text{nm}$ ($E_{27} \approx 42\,\text{eV}$) as the most intense. The several sample positioning axes enable the placement of the sample in (x, y, z) at the focus of an ellipsoidal mirror, the control of the nominal grazing angle θ, the nominal angular position of an in-vacuum camera 2θ, and the nominal orientation of the patterned features relative to the plane of incidence, or "face rotation" θ_{face}. During data collection, exposure times for the CCD are set to nearly saturate the camera in the 0th order (the brightest diffracted beam), thereby maximizing the dynamic range and SNR of each diffraction measurement.

A key distinction of this present work is the attempt to measure multiple 193 nm-immersion-printed metrology targets in a systematic study of EUV diffraction and its comparability to more established metrologies. A schematic view of this set of four periodic structures is illustrated as Fig. 2(a). These line:space arrays are all nominally 1:1 duty cycle with nominal pitches varying from $p = 100$ nm to $p = 114$ nm, yielding nominal CD differences of 2 nm to 3 nm. Samples are denoted LnnPmmm, where the nominal width is nn nm and pitch is mmm nm. Each target is 800 μm $\times$ 800 μm, ensuring underfilling of the target for both EUV diffractometry and CD-SAXS. Cross-sectional scanning electron micrographs (XSEM) (for similarly processed targets from this reticle) have yielded approximately 100 nm line heights.[23] Figure 2(b) illustrates the nominal angles for the EUV diffractometry measurements: the grazing angle θ and the "face rotation" θ_{face} which is the orientation of the patterned grating with respect to the plane of incidence.

Understanding these diffraction patterns requires an assessment of whether diffraction is observable for a given θ, θ_{face}, and h. For a small face rotation $\theta_{face} = \delta\theta_{\text{rot}}$, the m^{th} diffraction order (at first order in the small

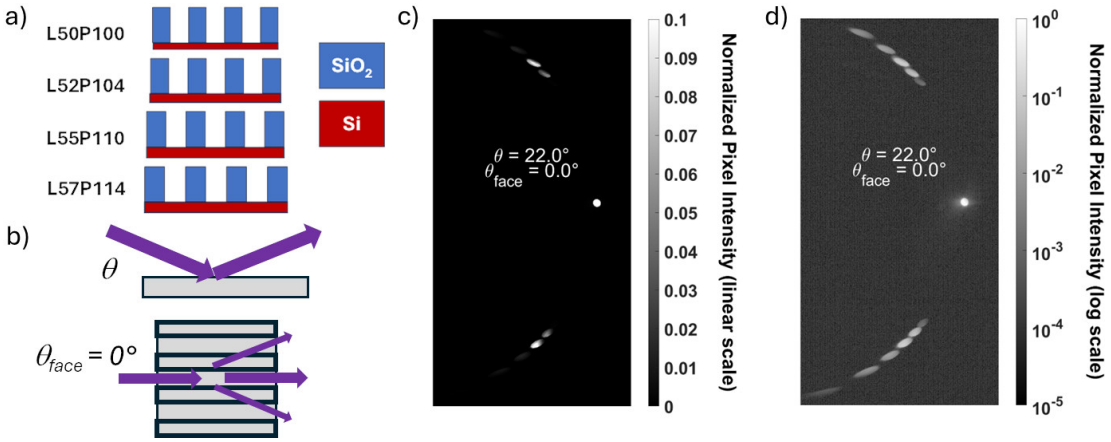

Figure 2. Metrology target set, relative orientations, and an example image from EUV diffractometry. a) Schematic layout for four periodic line-space arrays of SiO_2 on Si. b) Key measurement angles. Nominal grazing angle θ is defined relative to the sample plane. Nominal face rotation here is $\theta_{face} = 0°$. c,d) Diffraction pattern observed for L52P104 at $\theta = 22°$.

angle) should appear if

$$\left| \cos\theta \ \delta\theta_{\text{rot}} + \frac{\lambda_h m}{p} \right| \leq |\sin\theta|, \tag{1}$$

where $\lambda_h = \lambda_{IR}/h$. This equation results from Eq. 4-6,25, found in Appendix C. A first observation using Eq. 1 is that variation in p among the metrology targets required readjustments in the range of θ measured. Each scan is 17 angles in 0.5° increments starting at $\theta = [15°, 14°, 14°, 13°]$ for $p = [100\,\text{nm}, 104\,\text{nm}, 110\,\text{nm}, 114\,\text{nm}]$ to capture the $m = \pm 1$ order from the $h = 31$ harmonic and to capture $h = 29, 27, etc.$ with increasing θ. A second observation is that only $m \in \{0, -1, +1\}$ are possible in this experiment at these grazing angles.

Figure 2(c,d) shows an example diffraction pattern from one location measured on L52P104 at $\theta = 22°$ that illustrates the clear differences between $m = 0$ and $m = \pm 1$ in this experiment. On a linear scale (Fig. 2(c)), there is one dominant harmonic, $h = 27$. On a log scale (Fig. 2(d)), there are twelve finite spots in this diffraction pattern, all falling on an arc within the frame of the in-vacuum charge-coupled device (CCD). The center right spot is $m = 0$ for all harmonics, while spots at top and bottom are the several $m = \pm 1$ corresponding to various harmonics. A third observation is that for $p = 104$ nm, $\theta = 22°$, six observed harmonics $h = 21, .., 31$ (mod 2) are expected. Here, one $h = 21$ spot falls cleanly outside the CCD frame; we note that finite diffraction spots may be partially clipped by the sample horizon or CCD frame at other combinations of $\{p, \theta\}$. Corrections for the finite beam are noted in Appx. B.

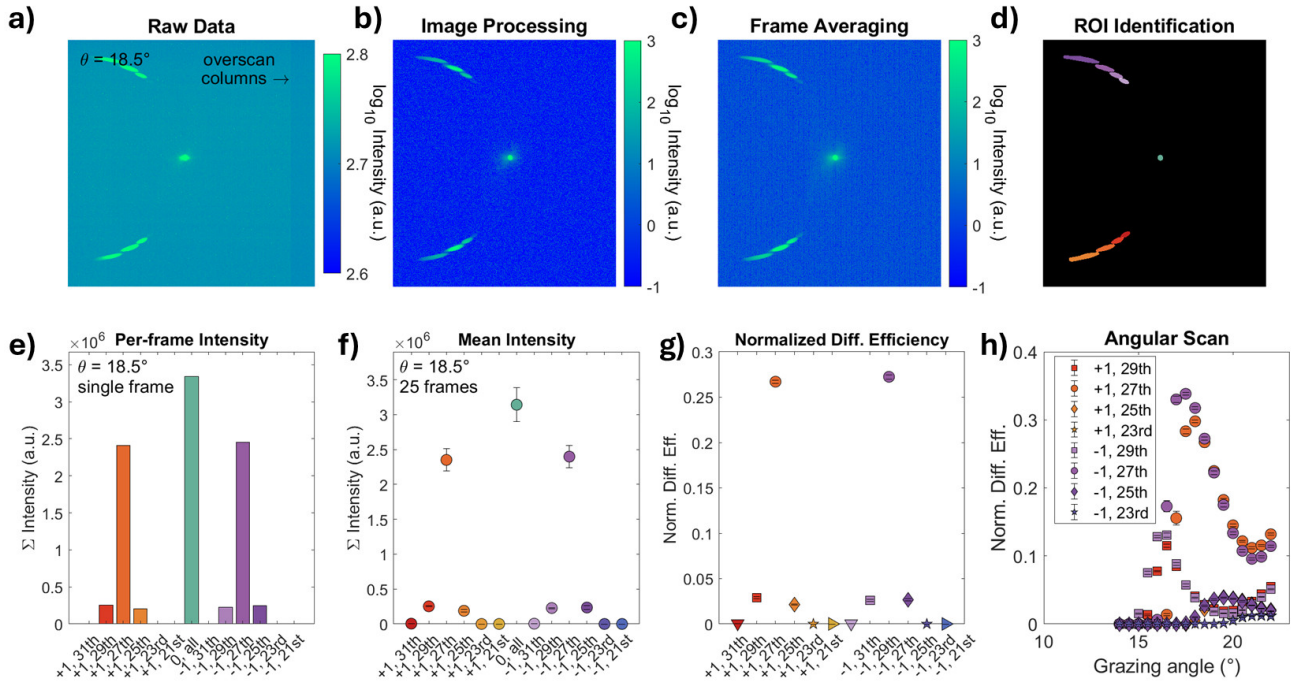

Figure 3. Key data reduction steps. Panels are either single frames or averages of 25 measurement locations. a) Raw Data - single frame with 2048 x 1848 pixels of data, 200 columns for overscan correction. b) Image Processing - single frame noise removal. c) Frame Averaging - Average of (b) over 25 locations. d) Region-of-interest (ROI) Identification - Extent of each finite spot from (c). e) Per-frame intensity - (d) applied to single frames, sum all intensities in ROIs. f) Mean intensity - Averages with respect to λ_h, m. g) Normalized Diffraction Efficiency - standard deviation reduced by normalization per-frame by 0th order. h) Angular Scan - data from (g) plotted with respect to grazing angle; used for fitting. Measurement error bars are 1σ, one standard deviation of the mean.

2.2 EUV diffraction: Analysis

Changes in the intensities of these spots are critical for our dimensional metrology, and accurate intensity measurement requires thorough data processing and data reduction steps. Procedures for addressing noise,

extracting intensities, and reporting data as function of θ for this instrument have been published recently[12,15] and summarized graphically in Fig. 3, with minor changes related to the multiple wavelengths. Referring again to Fig. 2(d), twelve regions of interest (ROI) are determined from thresholding to allow the summation of the intensities within each individual spot. These intensity sums I are indexed by target name, location index i, θ, m, and λ (for $m \neq 0$), as shown in Fig. 3(e) for L50P100 at $\theta = 18.5°$. To reduce measurement uncertainties, these $m = \pm 1$ intensity data are normalized within a single frame (i.e., for each i) against the $m = 0$ order to yield the normalized diffraction efficiency, or NDE, as

$$\mathsf{NDE}(i, m, \theta, \lambda) = \frac{I(i, m, \theta, \lambda)}{I(i, m = 0, \theta)}, m \neq 0. \tag{2}$$

Next, the mean and standard deviation over the 25 i locations for each target yield $\mathsf{NDE}(m, \theta, \lambda)$, which is the key quantity fitted against using electromagnetic simulations, corresponding with Figs. 3(g-h).

Briefly, Fig. 3(h) is important as it shows that the curves of $\mathsf{NDE}(m = -1, \theta)$ are displaced in θ relative to $\mathsf{NDE}(m = +1, \theta)$. Qualitatively, this is direct indicator of imperfect alignment of the sample relative to nominal values and motivates the inclusion of a perturbation term such as $\cos\theta\ \delta\theta_{\text{rot}}$ within Eq. 1.

2.3 EUV diffraction: Simulation and parametrization

Determination of the critical dimensions of these metrology targets from EUV diffractometry is an inverse problem requiring forward solutions from electromagnetic simulations that are indexed to a set of parameters. These simulations have been performed using `pySCATMECH`,[24,25] a `python` implementation of the SCATMECH[26] library. Specifically, we employed rigorous coupled wave analysis (RCWA) of gratings, exploiting the periodicity of these metrology targets. The non-linear regression fit to these data has been performed using `scipy.optimize.least_squares`[27] using the Trust Region Reflective algorithm.

For parametrization, a simple geometrical model has been developed for the cross-sections of these lines, inspired from XSEM from other coupons. Five floating geometrical parameters are the key quantities of interest, shown in Fig. 4(a). As mentioned earlier, the geometry of the EUV Imaging Reflectometer chamber precluded attempts to directly quantify the relative intensities of the HHG spectral comb, necessitating the floating of intensity ratios r_h for each target, $r_h = I_h / I_{27}, (h = 21, 23, 25, 29)$; the "spectral comb" in Fig. 4(b) is pseudodata, and $r_{31} \equiv 0$ as the weakest of the observed harmonics. We address approaches to mitigate or remove these r_h floated parameters in Sec. 3.3. The wavelength-dependent optical constants in this work are taken from the literature.[28]

The strong sensitivity of these EUV diffractometry measurements to alignment has been a central issue in performing fits to these data and defining the parametrization. Note, EUV diffractometry is much more sensitive

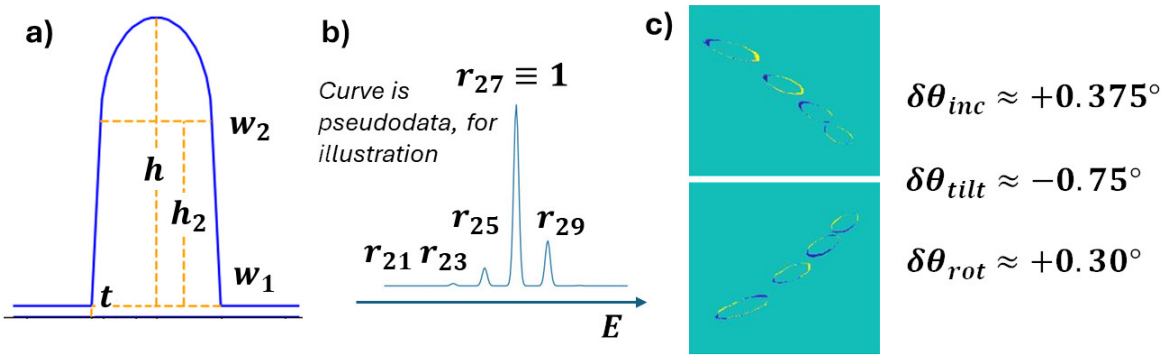

Figure 4. Parameterization of these targets and the experimental conditions. a) Geometrical parametrization for each target. Parameter t is in common among the four targets. b) Motivation for parameterizing the ratios r_h between the h^{th} and 27^{th} intensities, which could not be observed directly in this experiment. c) Difference images of the calculated versus observed $m = \pm 1$ orders for $h = 23, 25, 27, 29$. This fit solves for face rotation $\delta\theta_{face}$ using correction angles $\delta\theta_{\text{inc}}$ and $\delta\theta_{\text{tilt}}$ that are defined and determined in Appendix C.

to such deviations than EUV ptychographic coherent diffractive imaging (CDI) of non-periodic samples, for which this prototype reflectometer was designed. A simplistic approach was first used to address mismatches between experimental and measured data. Specifically, an additive incidence angle $\theta + \Delta\theta$ was considered to align the observed and predicted onsets of diffraction with wavelength, and the misalignment in θ for $\mathsf{NDE}(m = \pm 1, \theta)$ led to a second floating parameter $\theta_{face} + \Delta\theta_{face}$. Using five grating dimensions, four r_h, $\Delta\theta$, and $\Delta\theta_{\text{face}}$, individual fits (not shown) have been performed for the measurements from each of the four targets. These yielded conflicting $\Delta\theta$ and $\Delta\theta_{\text{face}}$, indicating an incomplete understanding of the experimental conditions.

We believe that the alignment of the sample should be consistent from target to target, therefore a different approach has been taken to determine if sample tilt further complicated this analysis. In Appendix C.1, this tilt is derived as three separate tilt angles $\{\delta\theta_{\text{inc}}, \delta\theta_{\text{tilt}}, \delta\theta_{\text{rot}}\}$ that should be common between target measurements; the oxide thickness should also be in common. One parallel sample fit has thus been performed for all four targets simultaneously with four common parameters and eight floating parameters per target (4 dimensional, 4 r_h), a total of 36 parameters for a fit of all four target geometries.

Optimizing fitted parametric values is somewhat sensitive to the starting points for the optimization, therefore aspects of the experimental dataset have been evaluated further to determine whether we can recover estimates of $\{\delta\theta_{\text{inc}}, \delta\theta_{\text{tilt}}, \delta\theta_{\text{rot}}\}$ prior to fitting the peak intensities with the simulated models. The zeroth order spot has been observed to walk across the CCD frame as the incidence angle is swept, attributable to tilt. This walking varies with θ_{face} and additional results are presented in Appendix C.2 to indicate $\delta\theta_{\text{tilt}} \approx -0.75^\circ$ and $\delta\theta_{\text{inc}} \approx 0.375^\circ$. The third angle is estimated in Appendix C.3 using sets of diffraction patterns such as Fig. 4(c) to calculate the required experimental conditions to match expected and observed diffraction patterns assuming $\delta\theta_{\text{tilt}}$ and $\delta\theta_{\text{inc}}$. This has yielded $\theta_{\text{rot}} \approx 0.3^\circ$ to enable our informed estimates for these three tilt angles. As the sample was mounted using a copper adhesive pad, the magnitude of these corrections is reasonable.

2.4 Critical dimension small angle X-ray scattering (CD-SAXS)

Critical dimension small angle X-ray scattering (CD-SAXS) is a variation on standard SAXS that can be used to characterize the detailed shape of periodic nanostructures. By rotating the sample relative to the incident beam, information on the vertical profile of the structure can be obtained. A CD-SAXS measurement is typically conducted by taking a scattering measurement at a series of incident angles and reconstructing the individual images into a reciprocal scattering map. This technique has been demonstrated on line gratings with complex shapes,[29] contact hole templates,[30] and has attracted significant interest for its ability to characterize tilt angles in high aspect ratio holes for memory.[31]

CD-SAXS measurements were conducted at the soft-matter interfaces (SMI) beamline at the National Synchrotron Light Source (NSLS-II). The incident energy was 16.1 keV and the beamsize was 200 µm × 30 µm. The

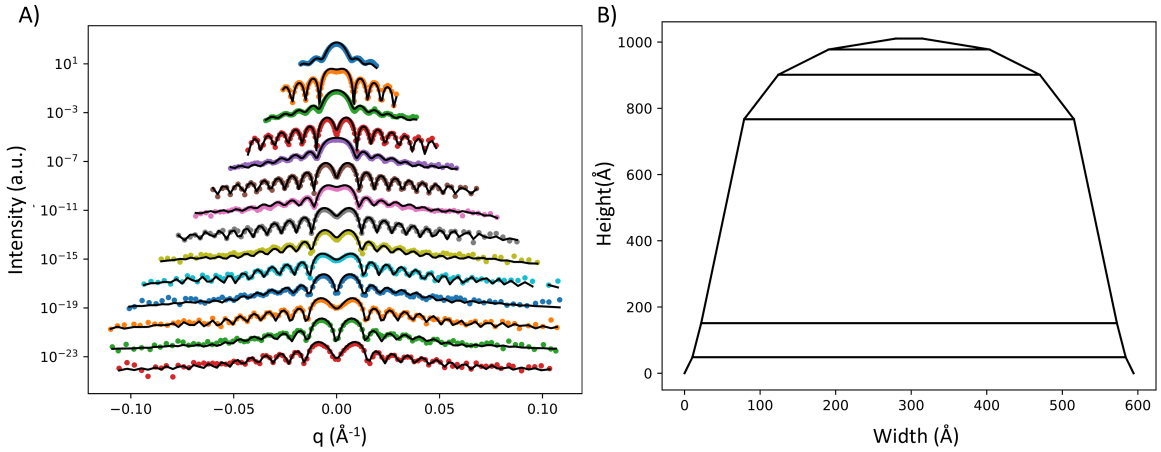

Figure 5. Representative CD-SAXS data, fit, and resultant geometry. a): Linecuts. Experimental data are shown in the colored circles, simulated data is shown in black lines. Data are arbitrarily scaled vertically for visual clarity. b) Six trapezoid geometric model used to simulate these scattering data.

sample-detector distance was 5 m and scattering patterns were collected at 1° intervals between -60° and +60°, where 0° is the sample normal. The data were corrected for the beam footprint size and absorption through the silicon. A representative scattering pattern after data reduction is shown in Fig. 5. The CD-SAXS data is simulated using a stack of symmetric trapezoids to describe the lineshape. The Fourier transform of a trapezoid has an analytical solution, enabling rapid iteration of the simulated scattering by varying the parameters of the trapezoid stack. Additional details on the fitting have been published previously.[31] In this case a differential evolution algorithm is used to conduct the initial optimization, followed by uncertainty analysis using a Markov Chain Monte Carlo algorithm. Figure 5(a) shows the linecuts from the scattering map, along with the simulated scattering from the model shown in Figure 5(b).

3. RESULTS AND DISCUSSION

3.1 EUV diffractometry fitting

Figure 6 shows the EUV diffraction intensity data from these four metrology targets and their fits, while the parametric values and uncertainties appear in Table 1. There is excellent agreement for three of the four metrology targets in Fig. 6. For these data, the most difficult aspects to match accurately are the NDE peak at $\theta \approx 18°$ for $h = 27$ and the NDE trough at $\theta \approx 21°$ for $h = 27$. Target L50P100 exhibits systematic error at these locations which may be due to variation of the incident beam direction or to an over-simplified geometry for this target. We note that the L50P100 was the first scan of a multi-day experiment. Since the other samples exhibit excellent agreement with CD-SAXS via our global fit, it is likely that thermalization of optics during the experiment could have induced small changes in the actual angle offsets between the gratings, such as variations in the ellipse orientation, sample mounting, or other upstream optics. Also, additional parameters may be needed for this target although five geometric parameters have yielded good fits for the other three targets. Adding a two-parameter trapezoid to an 11-parameter fit for L50P100 however led to multiple local minima (not shown) in a Markov Chain Monte Carlo calculation, with the closest fits yielding an unreasonably narrow bottom width < 10 nm.

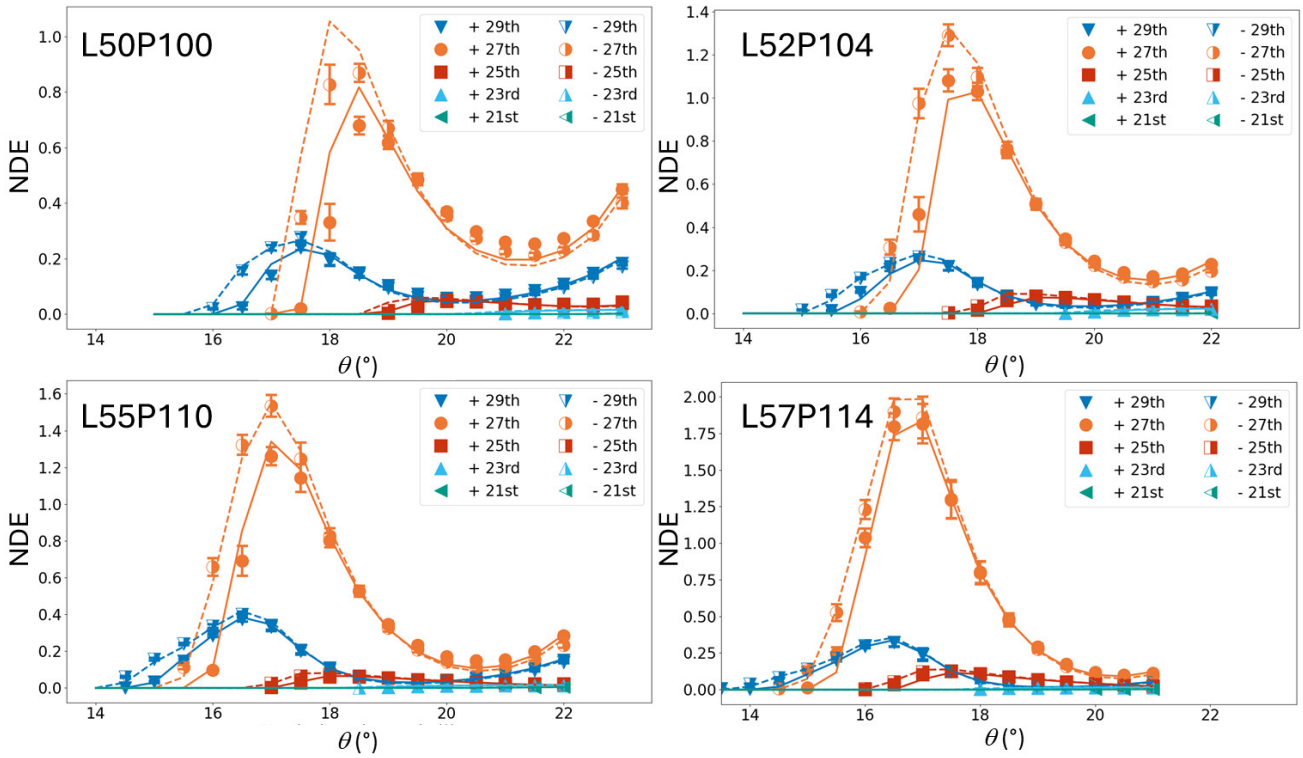

Figure 6. Fitted EUV diffractometry data. Simulated values (solid lines) are fitted against the experimental data (markers with 1σ errorbars) for both $m = \pm 1$.

Table 1. Parametric values and single standard deviation parametric uncertainties from parallel regression of EUV diffractometry data.

	w_1 (nm)	w_2 (nm)	h (nm)	h_2 (nm)
L50P100	43.1 ± 2.1	37.7 ± 2.1	99.7 ± 0.7	67.4 ± 3.8
L52P104	47.1 ± 3.2	42.9 ± 1.9	102.6 ± 0.8	55.2 ± 4.6
L55P110	46.4 ± 0.9	46.4 ± 1.3	102.5 ± 0.6	59.2 ± 5.9
L57P114	52.1 ± 1.6	48.2 ± 4.0	103.6 ± 1.5	59.4 ± 17.8
	t (nm)	$\delta\theta_{inc}$(°)	$\delta\theta_{tilt}$(°)	$\delta\theta_{rot}$(°)
common	3.8 ± 0.4	0.407 ± 0.000	-0.708 ± 0.000	0.429 ± 0.000
	r_{29}	r_{25}	r_{23}	r_{21}
L50P100	0.257 ± 0.005	0.095 ± 0.004	0.020 ± 0.003	0.003 ± 0.005
L52P104	0.213 ± 0.004	0.125 ± 0.004	0.031 ± 0.003	0.001 ± 0.008
L55P110	0.275 ± 0.005	0.090 ± 0.003	0.022 ± 0.003	0.005 ± 0.003
L57P114	0.177 ± 0.004	0.113 ± 0.003	0.025 ± 0.003	0.005 ± 0.005

A review of the parametric values and uncertainties in Table 1 shows that the mid-width value w_2 increases monotonically with increasing nominal linewidth as expected, and that the bottom width w_1 only deviates from this trend for L55P110. Note that there are large uncertainties associated with the h_2 parameter, meaning that this experiment is insensitive to the precise determination of where the half-ellipse ends and the trapezoid begins. Furthermore, while the ratios r_h appears to be well-defined (i.e. low uncertainty) within a scan, note that these differ greatly among scans and further study is required. Moving forward, direct monitoring of relative harmonic intensities or the use of filtered harmonics can be used to exclude these parameters from the fits.

3.2 EUV diffractometry vs CD-SAXS: Comparisons

EUV diffractometry and CD-SAXS both yield cross-sectional geometries for these periodic structures. Figure 7 presents our first comparison between EUV diffractometry and CD-SAXS. Here, 2000 samples were drawn from a multivariate normal distribution with mean μ and covariance Σ to illustrate the uncertainties in the EUV diffractometry profile. The mean and covariance are calculated from the fit. The difference between the two sets of measurements likely arises from incomplete knowledge of the sample, experimental conditions that limits our model fits, as well as potential systematic errors in either or both techniques. A key qualitative point of agreement between the synchrotron-based CD-SAXS and table-top EUV diffractometry is critical dimension linewidth at mid-height across the set of four metrology targets. A systematic trend is that the EUV diffractometry cross-section consistently under-reports the bottom width relative to CD-SAXS, likely due to an insufficient EUV geometrical model. The CD-SAXS total height falls within the EUV uncertainty profile for two of the four geometries but with disagreement at the extremes (L50P100 and L57P114). The near agreement throughout between the profiles for L52P104, even with limitations in the EUV geometry profiles, is highly encouraging though more needs to be done to ensure better fits across such sets.

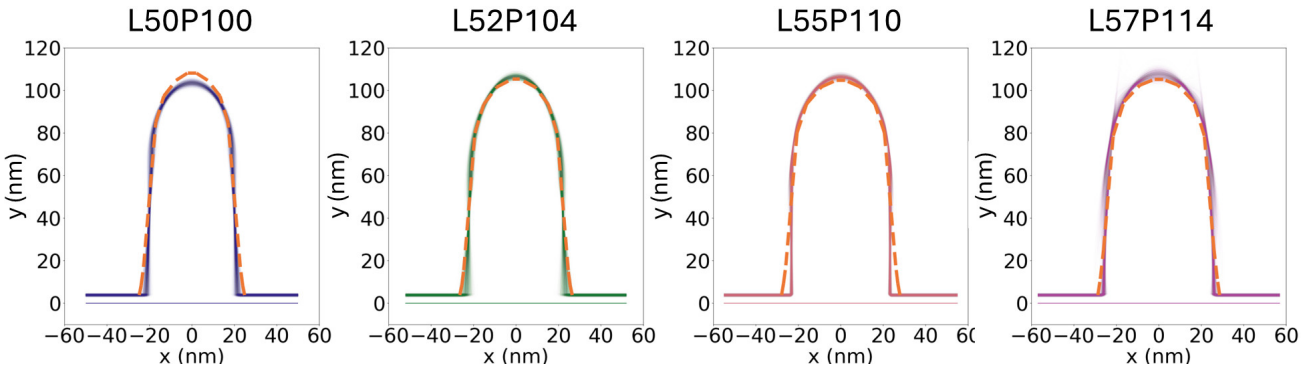

Figure 7. EUV fitted cross-sections (solid lines) vs. CD-SAXS geometries (orange dashed lines). EUV cross-sections presented with its uncertainty envelope. The CD-SAXS uncertainties fall within the width of the line.

The potential of EUV diffractometry is demonstrated quantitatively in Fig. 8 as the width of the EUV diffractometry profiles at 50 % of the EUV diffractometry total height are shown as functions of measured CD-SAXS line widths at 50 % total CD-SAXS height. There is already a strong correlation between these two non-destructive techniques. We believe that these comparisons should motivate new experiments towards the higher throughput and industrially relevant length scales needed by the industry.

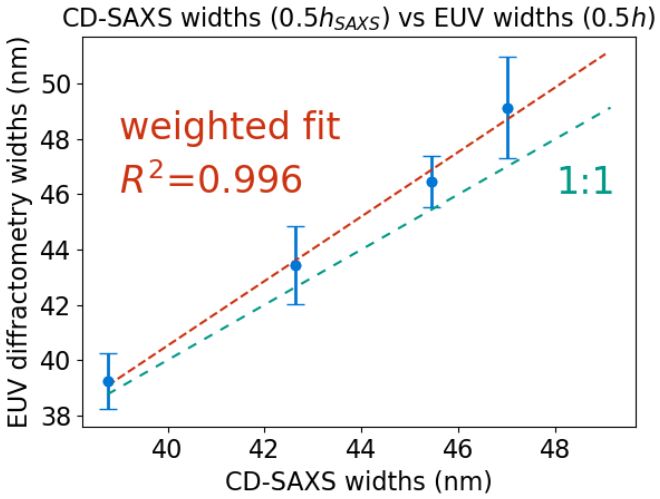

Figure 8. EUV width at $0.5h$ with 1σ distribution widths, determined from 100 realizations as in Fig. 7, as a function of CD-SAXS width at $0.5h$ of CD-SAXS.

3.3 Improving upon these results

EUV diffractometry is a powerful approach for characterizing dimensions of industrially relevant structures. Key aspects can be addressed in a dedicated CD metrology EUV HHG-based instrument: in-situ measurement of the HHG wavelengths, in-situ monitoring of the relative harmonic intensities, and accurate sample mounting.

There are several approaches to dispensing with the four floating parameters r_h per metrology target. A calibrated spectrometer with access to the incident beam that can measure these relative intensities is the most straightforward approach for reaping the benefits of multi-wavelength simultaneous measurements. Methods to move back and forth between the optional filtering of the spectral comb to pass a single harmonic is another approach to remove the ambiguities in this study, while preserving many of the benefits of multi-wavelength measurements. Filtering can be performed using enhanced wavelength-selective EUV mirrors (planned for CU-Boulder) or using a monochromator (being installed at NIST) to implement EUV diffractometry at each harmonic separately.

This experiment has also challenged us to reconsider the tolerances required for sample positioning and its correction. The fullest mitigation of sample tilt would require both protocols for measuring tilt and also vacuum compatible tilt stage(s) for correction, with iteration. While the EUV Imaging Reflectometer was initially designed for general purpose EUV ptychography, future dedicated CD EUV diffractometry experiments will require additional automation. One axis of tilt correction is being implemented on the new experimental chamber at NIST Gaithersburg. Even if tilt correction stages are not available, new methods for ascertaining this tilt are needed; as proposed in Appendix C.3, small data sets can be collected at least three different values of θ_{face} to allow for better estimation of these tilt angles.

At the University of Colorado, a state-of-the-art HHG system will allow for precise tuning and shaping of the EUV comb.[16,32] NIST is also pairing a new HHG front-end to a new ellipsometer/diffractometer chamber currently under development and will be calibrating a commercial spectrometer for characterization at several points along the beamline. The NIST system, designed to interrogate semiconductor samples, features the capability to change the polarization of the HHG head from s-polarization to p-polarization without breaking vacuum. We

envision even greater accuracy for these measurements through access to these orthogonal polarization states for patterned gratings.

4. CONCLUSION

Four line-space targets patterned using an industrial metrology reticle have been successfully measured harnessing extreme ultraviolet diffractometry using an in-laboratory coherent high-harmonic generation extreme ultraviolet laser. Five wavelengths of light between $\lambda_{\min} = 27.4$ nm and $\lambda_{\max} = 37.4$ nm yielded $m = \pm 1$ diffraction orders that have been measured as functions of grazing angle. Dimensions for these targets were determined through electromagnetic simulations that utilized parameterized geometrical cross-sections, intensity ratios, and a triplet of sample tilt angles held in common across these four targets. The resulting parametrized cross-sections from EUV diffractometry compare favorably with those from CD-SAXS; although quantitative discrepancies are found in the bottom line width and height, line widths at half height have been shown to be highly correlated.

ACKNOWLEDGMENTS

This work was performed with funding from the CHIPS Metrology Program, part of CHIPS for America, National Institute of Standards and Technology, U.S. Department of Commerce.

REFERENCES

[1] "International roadmap for devices and systems (IRDS™) 2022 edition: Metrology." https://irds.ieee.org/editions/2022/metrology (2022). Accessed 6 Sept 2024.

[2] Fan, T. et al., "Bright circularly polarized soft X-ray high harmonics for X-ray magnetic circular dichroism," *Proceedings of the National Academy of Sciences* **112**(46), 14206–14211 (2015). https://doi.org/10.1073/pnas.1519666112.

[3] Huang, P.-C. et al., "Polarization control of isolated high-harmonic pulses," *Nature Photonics* **12**(6), 349–354 (2018). https://doi.org/10.1038/s41566-018-0145-0.

[4] Gross, H., Rathsfeld, A., Scholze, F., and Bär, M., "Profile reconstruction in extreme ultraviolet (EUV) scatterometry: modeling and uncertainty estimates," *Measurement Science and Technology* **20**(10), 105102 (2009). https://doi.org/10.1088/0957-0233/20/10/105102.

[5] Herrero, A. F., Pflüger, M., Puls, J., Scholze, F., and Soltwisch, V., "Uncertainties in the reconstruction of nanostructures in EUV scatterometry and grazing incidence small-angle X-ray scattering," *Opt. Express* **29**, 35580–35591 (Oct 2021). https://doi.org/10.1364/OE.430416.

[6] Lohr, L. M., Ciesielski, R., Glabisch, S., Schröder, S., Brose, S., and Soltwisch, V., "Nanoscale grating characterization using EUV scatterometry and soft x-ray scattering with plasma and synchrotron radiation," *Appl. Opt.* **62**, 117–132 (Jan 2023). https://doi.org/10.1364/AO.475566.

[7] Bahrenberg, L., Danylyuk, S., Glabisch, S., Ghafoori, M., Schröder, S., Brose, S., Stollenwerk, J., and Loosen, P., "Characterization of nanoscale gratings by spectroscopic reflectometry in the extreme ultraviolet with a stand-alone setup," *Opt. Express* **28**(14), 20489–20502 (2020). https://doi.org/10.1364/OE.396001.

[8] Ku, Y.-S., Yeh, C.-L., Chen, Y.-C., Lo, C.-W., Wang, W.-T., and Chen, M.-C., "EUV scatterometer with a high-harmonic-generation EUV source," *Opt. Express* **24**(24), 28014–28025 (2016). https://doi.org/10.1364/OE.24.028014.

[9] Gardner, D. F., Tanksalvala, M., Shanblatt, E. R., Zhang, X., Galloway, B. R., Porter, C. L., Karl, Jr., R., Bevis, C., Adams, D. E., Kapteyn, H. C., Murnane, M., and Mancini, G. F., "Subwavelength coherent imaging of periodic samples using a 13.5 nm tabletop high-harmonic light source," *Nature Photonics* **11**(4), 259+ (2017). https://doi.org/10.1038/NPHOTON.2017.33.

[10] Tanksalvala, M. et al., "Complex imaging reflectometry for dopant profile measurements using tabletop high harmonic light," in [*Imaging and Applied Optics 2019 (COSI, IS, MATH, pcAOP)*], CW3A.6, Optica Publishing Group (2019). https://doi.org/10.1364/COSI.2019.CW3A.6.

[11] Jenkins, N. W. et al., "Ptychographic phase-sensitive imaging reflectometry for depth-resolved nanostructure characterization using tabletop euv light," in [*OSA High-brightness Sources and Light-driven Interactions Congress 2020 (EUVXRAY, HILAS, MICS)*], EW3A.4, Optica Publishing Group (2020). https://doi.org/10.1364/EUVXRAY.2020.EW3A.4.

[12] Tanksalvala, M. et al., "Nondestructive, high-resolution, chemically specific 3D nanostructure characterization using phase-sensitive EUV imaging reflectometry," *Science Advances* **7**(5), eabd9667 (2021). https://doi.org/10.1126/sciadv.abd9667.

[13] Wang, B., Brooks, N., Tanksalvala, M., Esashi, Y., Jenkins, N., Johnsen, P., Binnie, I., Gui, G., Shao, Y., Murnane, M. M., and Kapteyn, H. C., "Robust and reliable actinic ptychographic imaging of highly periodic structures in EUV photomasks," *Proc. SPIE* **12293**, 122930D (2022). https://doi.org/10.1117/12.2641726.

[14] Porter, C. et al., "Soft x-ray: novel metrology for 3D profilometry and device pitch overlay," *Proc. SPIE* **12496**, 124961I (2023). https://doi.org/10.1117/12.2658495.

[15] Esashi, Y., Jenkins, N. W., Shao, Y., Shaw, J. M., Park, S., Murnane, M. M., Kapteyn, H. C., and Tanksalvala, M., "Tabletop extreme ultraviolet reflectometer for quantitative nanoscale reflectometry, scatterometry, and imaging," *Review of Scientific Instruments* **94**, 123705 (12 2023). https://doi.org/10.1063/5.0175860.

[16] Klein, C., Jenkins, N., Shao, Y., Li, Y., Park, S., Kim, W., Kapteyn, H., and Murnane, M., "Extreme ultraviolet scatterometry for characterizing nanometer scale features in a damascene sample," in [*Frontiers in Optics + Laser Science 2024 (FiO, LS)*], FTu1B.2, Optica Publishing Group (2024). https://doi.org/10.1364/FIO.2024.FTu1B.2.

[17] Perera, C. N., Houser, D. C., Murray, C. G., Khodarev, A. N., and Grodt, T. W., [*EUV microscope*], U.S. Patent 12,203,874 (2025).

[18] Germer, T. A., [*Mueller Matrix Ellipsometer*], U.S. Patent Application 2024/0011894 (2024).

[19] Tarrio, C., Grantham, S., Vest, R. E., Germer, T. A., Barnes, B. M., Moffitt, S. L., Simonds, B. J., and Spidell, M., "NIST efforts in extreme-ultraviolet metrology," *Proc. SPIE* **12750**, 127500F (2023). https://doi.org/10.1117/12.2686832.

[20] Moffitt, S. L., Barnes, B. M., Germer, T. A., Grantham, S., Shirley, E. L., Sohn, M. Y., Sunday, D. F., and Tarrio, C., "Instrument development for spectroscopic ellipsometry and diffractometry in the EUV," in [*Frontiers of Characterization and Metrology for Nanoelectronics: 2024*], (2024).

[21] Bunday, B. D., "Metrology test artifact availability improvement," *Proc. SPIE* **12053**, 120531C (2022). https://doi.org/10.1117/12.2615726.

[22] Kapteyn, H. C. et al., "Coherent EUV Light Sources Based on High-Order Harmonic Generation: Principles and Applications in Nanotechnology," in [*Photon Sources for Lithography and Metrology*], Bakshi, V., ed., ch. 21, SPIE (September 2023). https://doi.org/10.1117/3.2638242.ch21.

[23] Bunday, Benjamin and Ball, Yvette, "100nm depth oxide HM (L50P100) Line & Space, navigation & results." `https://cdn.shopify.com/s/files/1/0587/4801/0555/files/AMAG7_100nm_HM_LineSpace_CD_results_Jan3.pdf` (2022). Accessed 22 Jul 2024.

[24] Germer, T. A., "pySCATMECH: a Python interface to the SCATMECH library of scattering codes," *Proc. SPIE* **11485**, 114850J (2020). https://doi.org/10.1117/12.2568578.

[25] "pySCATMECH." `http://github.com/usnistgov/pySCATMECH` (2020).

[26] "SCATMECH: Polarized Light Scattering C++ Class Library." `https://pages.nist.gov/SCATMECH/index.htm` (2020).

[27] Virtanen et al., P., "SciPy 1.0: Fundamental Algorithms for Scientific Computing in Python," *Nature Methods* **17**, 261–272 (2020). https://doi.org/10.1038/s41592-019-0686-2.

[28] Palik, E. D., [*Handbook of optical constants of solids*], vol. 3, Academic Press (1998).

[29] Sunday, D. F., List, S., Chawla, J. S., and Kline, R. J., "Determining the shape and periodicity of nanostructures using small-angle X-ray scattering," *Journal of Applied Crystallography* **48**(5), 1355–1363 (2015). https://doi.org/10.1107/S1600576715013369.

[30] Sunday, D. F., Delachat, F., Gharbi, A., Freychet, G., Liman, C. D., Tiron, R., and Kline, R. J., "X-ray characterization of contact holes for block copolymer lithography," *Journal of Applied Crystallography* **52**(1), 106–114 (2019). https://doi.org/10.1107/S1600576718017272.

[31] Thompson, W. D., Kline, R. J., Sunday, D. F., Wu, W., Sorkhabi, O., Zhang, J., and Chen, X., [*Determining tilt angle in patterned arrays of high aspect-ratio structures by small-angle X-ray scattering*], U.S. Patent 11,181,489 (2021).

[32] Klein, C., Jenkins, N., Shao, Y., Li, Y., Park, S., Kim, W., Kapteyn, H., and Murnane, M., "Coherent EUV scatterometry of the profiles of 2D periodic structures with mathematically optimal experiemental design," in preparation.

[33] Germer, T. and Patrick, H., "Effect of bandwidth and numerical aperture in optical scatterometry," *Proc. SPIE* **7638**, 76381F (2010). https://doi.org/10.1117/12.846776.

APPENDIX A: EUV HHG DETAILS

A Ti:Sapphire regenerative amplifier provides 38 fs pulses at a 3 kHz repetition rate, with central wavelength at 795 nm and pulse energy up to 2.6 mJ. We utilize a fraction of the laser energy (≈ 0.83 mJ) and focus it into Ar gas (≈ 5.6 kPa (42 Torr)) to generate coherent extreme ultraviolet light via HHG around photon energies $E \approx 41.5$ eV. The rest of the beamline is kept at a vacuum of $P < 1 \times 10^5$ Torr to prevent absorption of the EUV light in air. A diagnostic EUV spectrometer (toroidal focusing mirror and a transmission grating) was used to optimize the phase-matching conditions by tuning Ar gas pressure and chirp of the driving laser.

For harmonics around 30 nm, Si rejectors, Al filters, and SiC/Mg multilayer mirrors are used to filter the EUV photons from the residual IR photons and shape the EUV spectral comb. The resulting beam has a flux of approximately 10^9 photons/s, with ≈ 92 % of its energy concentrated in the 27th harmonic and the remaining energy in adjacent harmonics. This beam is focused using an ellipsoidal mirror onto the sample. The reflected sample diffraction is measured with an in-vacuum CCD camera (see Fig. 1) positioned 32 mm from the sample.

Note that this HHG flux is far below the typical flux of 10^{12} photons/s at 30 nm using more modern HHG designs, which were not needed in the prototype EUV reflectometer at CU-Boulder, since the ptychographic imaging rate was limited by the CCD readout. This older design is now being replaced with a state-of-the art laser and HHG system.[22]

APPENDIX B: FINITE BEAM EFFECTS

The beam has a finite profile, a conical spread of approximately 0.5°. As the diffracted beams approach grazing angle 0°, the diffraction dots elongate and are not well approximated by their average angle of incidence. To partially alleviate this, we approximate the beam with three angles of incidence and average the results:[33]

$$DE'(\theta) = 0.3DE(\theta + 0.25^\circ) + 0.4DE(\theta) + 0.3DE(\theta - 0.25^\circ). \tag{3}$$

The coefficients $0.3, 0.4, 0.3$ were calculated by integrating the beam profile over the corresponding angle of incidences. The parameters of the grating are determined by minimizing the least squares function. The parametric uncertainties are determined by inverting the Hessian matrix evaluated at the best fit values.

The finite profile of the beam offers a secondary challenge. For smaller grazing angles, some of the diffraction orders are partially cut off by the horizon. The full diffraction spot does not appear on the camera, and thus the simulated values are not expected to match the experimentally measured value. The intensities of the cut off diffraction spots are extremely weak, but their standard deviations are still roughly proportional to their intensities, meaning the cut off spots yield a large error in the least-squares cost function. To account for this mismatch, we implement a 'soft rejection', in which a small number, chosen to be 0.005, is added to the standard deviation of the diffraction efficiencies. This slight increase of the standard deviation will reduce the importance of the weakest intensities on the least squares fit.

APPENDIX C: TILT ANGLES

C.1 Tilt geometry

In Fig. 2(b), two nominal angles have been defined, the grazing angle θ and the face rotation θ_{face}. In order to mitigate imperfections in sample mounting and alignment, the geometry of this diffractometry experiment must be explored in greater detail to incorporate tilt. The incoming beam has propagation vector

$$\hat{k} = (\cos\theta, 0, -\sin\theta), \tag{4}$$

and reflects off the sample. Nominally, the sample is mounted so its normal is in the $\hat{z}$ direction, but in general this is not the case; the sample can be mounted with a small tilt that can be described using three small angles. These encode the sample tilt, as depicted in Fig. 9, by three orthonormal vectors: the normal $\hat{n}$, and two perpendicular axes $\hat{m}$ and $\hat{q}$ that lie in the sample plane as shown in Fig. 9. The one-dimensional grating is periodic along $\hat{m}$, and uniform along $\hat{q}$:

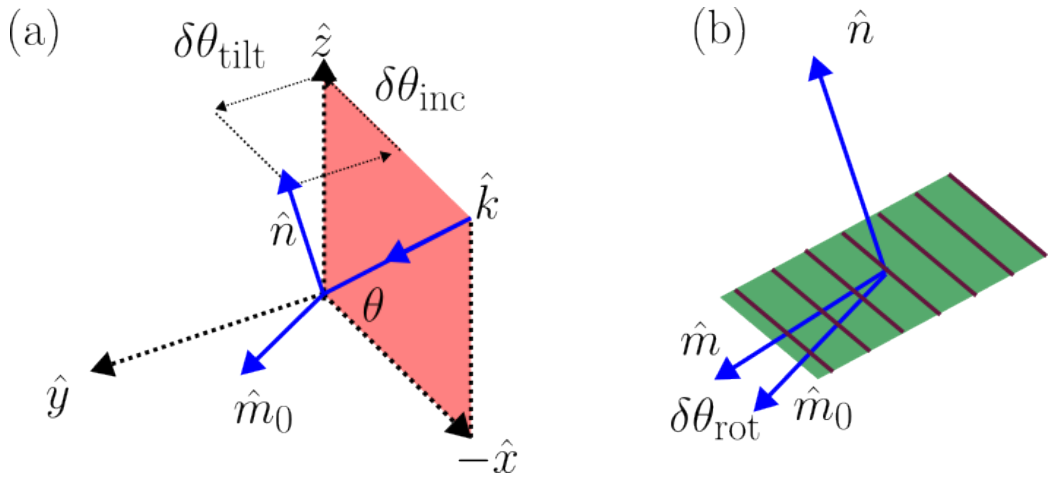

Figure 9. Definition of the tilt angles.

$$\hat{q} = (1, -\delta\theta_{\text{rot}}, -\delta\theta_{\text{inc}}) \tag{5}$$
$$\hat{m} = (\delta\theta_{\text{rot}}, 1, -\delta\theta_{\text{tilt}}) \tag{6}$$
$$\hat{n} = (\delta\theta_{\text{inc}}, \delta\theta_{\text{tilt}}, 1) \tag{7}$$

The angle the beam makes with the sample is the true incident angle, which we convert to the true grazing angle θ_{grazing}:

$$-\cos\theta_{\text{incident}} = \hat{n}\cdot\hat{k} \tag{8}$$
$$= \delta\theta_{\text{incident}}\cos\theta - \sin\theta \tag{9}$$
$$\theta_{\text{incident}} = \frac{\pi}{2} - \theta + \delta\theta_{\text{inc}} \tag{10}$$
$$\theta_{\text{grazing}} = \theta - \delta\theta_{\text{inc}} \tag{11}$$

The true grazing angle of the beam is the nominal angle minus the tilt of the normal in the xz-plane.

The face rotation of the sample is also affected by tilt. A diffractometer will report 0° face rotation when the beam $\hat{k}$ is perfectly in plane with $\hat{n}$ and $\hat{q}$. We will denote this reference frame with the three orthonormal vectors $\hat{n}$, $\hat{q}_0$, $\hat{m}_0$, which read

$$\hat{q}_0 = (1, \delta\theta_{\text{tilt}} \tan\theta, -\delta\theta_{\text{inc}}) \tag{12}$$
$$\hat{m}_0 = (-\delta\theta_{\text{tilt}} \tan\theta, 1, -\delta\theta_{\text{tilt}}) \tag{13}$$
$$\hat{n} = (\delta\theta_{\text{inc}}, \delta\theta_{\text{tilt}}, 1) \tag{14}$$

The actual face rotation is thus

$$\hat{m} - \hat{m}_0 = \delta\theta_{\text{rot}} + \delta\theta_{\text{tilt}} \tan\theta. \tag{15}$$

Finally, the polarization of the incoming light is affected. As the sample is tilted, the polarization of the light is no longer s-polarized, but s-polarized plus a small rotation. The Stokes vector reads

$$(1, 1, \delta\psi, 0), \tag{16}$$

where the small rotation $\delta\psi$ can be expressed in terms of the sample tilt. However, because the grating is symmetric about reflection in the xz plane to first order, this correction enters the calculation of the diffraction efficiencies at second order, and thus can be safely ignored.

C.2 Zeroth order spot location

To extract the tilt angles of the sample, we turn to a geometric calculation that predicts how the central, zeroth order spot will walk across the camera as the incidence angle is swept, if the sample is tilted.

If the incident beam has wavevector $\hat{k}$, then the reflected beam has wavevector $\hat{K}$

$$\begin{aligned}\hat{K} &= \hat{k} - 2(\hat{k} \cdot \hat{n})\hat{n} \\ &= (\cos\theta + 2\delta\theta_{\text{inc}} \sin\theta, 2\delta\theta_{\text{tilt}} \sin\theta, \sin\theta - 2\delta\theta_{\text{inc}} \cos\theta)\end{aligned} \tag{17}$$

with $\hat{n}$ the normal of the sample.

The $\hat{y}$ component of the reflected beam $\hat{K}$ is proportional to $\sin\theta$. As the grazing angle is swept, the location of the central beam on the CCD camera will travel. This observation allows us to extract the tilt angle from the CCD images: by tracking how the location of the zeroth order dot evolves with θ. The location of the dot was extracted from the images and plotted in Fig. 10. In addition, the drifts of the central beam were also recorded when the sample's face was rotated by 15°. This allowed us to extract $\delta\theta_{\text{inc}}$ as well as $\delta\theta_{\text{tilt}}$:

$$\delta\theta'_{\text{tilt}} = \delta\theta_{\text{tilt}} \cos\theta_{\text{face}} + \delta\theta_{\text{inc}} \sin\theta_{\text{face}} \tag{18}$$
$$\delta\theta'_{\text{inc}} = -\delta\theta_{\text{tilt}} \sin\theta_{\text{face}} + \delta\theta_{\text{inc}} \cos\theta_{\text{face}}, \tag{19}$$

where $\varphi = 15°$.

For the 0° data, the Y coordinate drifts approximately 8 pixels, while for the 15° data it appears to drift approximately 9 pixels. Using the fact that the camera is approximately 2500 pixels from the sample, the tilts read

$$\delta\theta_{\text{tilt}} = -0.75° \tag{20}$$
$$\delta\theta_{\text{inc}} = 0.375°. \tag{21}$$

For future experiments, measuring at more face rotation angles will be beneficial. The calculation ignores any imperfections in the machine; a misalignment of the arms that control the grazing angle and camera angle can replicate a Y-coordinate drift. To eliminate such possibilities, we propose measuring the drift with more than two rotation angles. Assume the Y-coordinate drift due to machine imperfections is given as $f(\theta)$, with no dependence on rotation angle θ_{face}.

The Y coordinate location reads

$$Y(\theta) = 2d \sin\theta(\delta\theta_{\text{tilt}} \cos\theta_{\text{face}} + \delta\theta_{\text{inc}} \sin\theta_{\text{face}}) + f(\theta), \tag{22}$$

where $d = 2500$ pixels. As the machine contribution $f(\theta)$ does not depend on θ_{face}, it can be removed with repeated measurements of the drift at different values of θ_{face}.

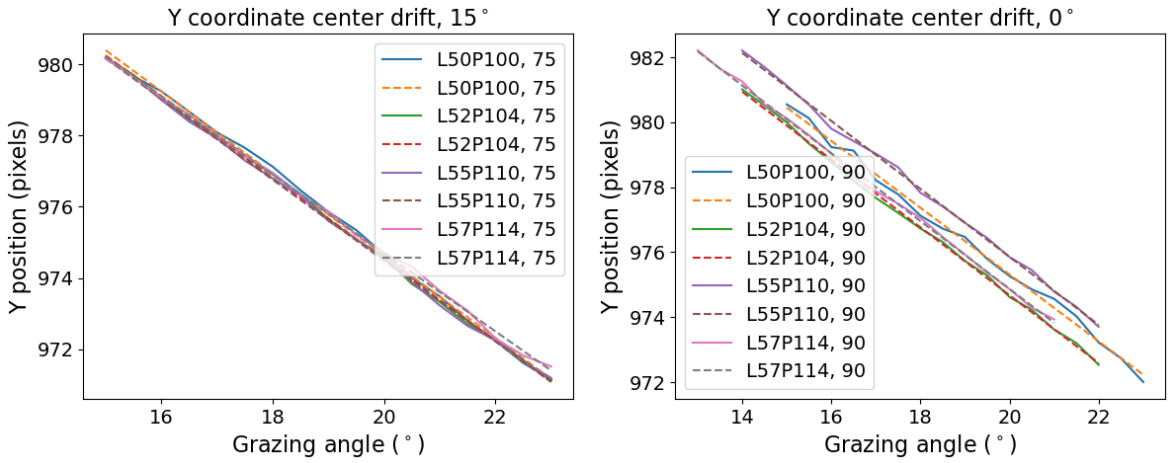

Figure 10. Drifts of the Y coordinate of the zeroth order beam as a function of incidence angle, for all datasets.

C.3 Recovering tilt angles from diffraction patterns

It is possible to recover a rough estimate of the tilt angles by observing the physical location of the diffraction dots as they appear on the CCD camera. An incoming beam with wavevector $\hat{k}$ can be decomposed into its components in the frame of the sample:

$$\hat{k} = (\hat{k} \cdot \hat{n})\hat{n} + (\hat{k} \cdot \hat{q})\hat{q} + (\hat{k} \cdot \hat{m})\hat{m}. \tag{23}$$

As the sample is uniform along $\hat{q}$, the corresponding component $\hat{k} \cdot \hat{q}$ is conserved. The sample is translation invariant with period a_0 along $\hat{m}$, so is conserved modulo $2\pi m/k_0 a_0$. The third component of the diffracted beam, the normal, is found by forcing the diffracted wavevector to have unit norm. If this is impossible, the beam does not exist. The diffracted wavevector with order m, $\hat{K}_m$, reads

$$\hat{K}_m = K_m^{\hat{n}}\hat{n} + (\hat{k} \cdot \hat{m} + \frac{2\pi m}{k_0 a_0})\hat{m} + (\hat{k} \cdot \hat{q})\hat{q}, \tag{24}$$

$$K_m^{\hat{n}} = \sqrt{1 - \left(\hat{k} \cdot \hat{m} + \frac{2\pi m}{k_0 a_0}\right)^2 - (\hat{k} \cdot \hat{q})^2}. \tag{25}$$

In order to calibrate the instrument when fitting the diffraction efficiencies, we utilize the geometric information in the diffraction patterns, namely the location and shape of each diffraction order. During the data taking, before and after each angle, we collect the un-reflected beam data with the sample out of the beam path and the camera at nominally 0 degrees. Since we align the red beam to be parallel to base of the instrument, the vertical offset of the centroid of the un-reflected beam should be calculated. The experimental diffraction patterns are shifted vertically so that the mismatch in this direction will only be due to the tilt of the sample normal around the horizontal axis. We then apply an adaptive threshold to the experimental diffraction patterns in order to preserve the shape of all the orders, each of which has varying intensities. The result of this pre-processing is a stack of binary masks for each target.

Our forward model for calculating the predicted binary diffraction pattern is parametrized by six variables: the sample-to-camera distance z, the driving laser wavelength-to-period ratio r, the three angles describing the deviation of the sample normal to the normal in the laboratory frame, and a global offset to the nominal camera angles that describes its deviation from the laboratory frame. A custom function is written to output the predicted binary masks and calculate the overlap error from the pre-processed experimental masks. Finally, a global optimization algorithm such as Genetic Algorithm (GA) is started to find the optimal set of six variables that maximizes the overlap.